



Passive control of the concentration boundary layer in microfluidic fuel cells using Dean vortices

Wiebke Rösing¹ · Toni Schildhauer¹ · Jörg König¹ · Christian Cierpka¹

Received: 19 March 2019 / Accepted: 7 August 2019 / Published online: 28 August 2019
© The Author(s) 2019

Abstract

Microfluidic fuel cells are limited by the formation of concentration boundary layers at the electrodes, resulting in low power density and low fuel utilization. This work demonstrates a novel method to enhance the diffusion-limited mass transport by decreasing the size of the concentration boundary layer using Dean vortices. These vortices are induced by a curved microchannel and enhance the mass transport of fresh reactant towards the electrodes. Numerical simulations were performed to show the influence of the Dean vortices on the performance of a microfluidic fuel cell. Furthermore, a curved microfluidic device with segmented electrodes was fabricated, which allows to experimentally investigate the effect of the enhanced diffusion-limited mass transport on the current density of a model redox couple and thus to prove the concept and the numerical results. It is shown that the Dean vortices, evolving in the curved channel, cause a convective transport of fresh solution towards the electrodes yielding a high current density and resulting in an improvement of 30% using a curved microfluidic fuel cell instead of a straight one. On condition that diffusive and convective mass transport are well-balanced, this approach promises not only a higher power density, but also a much higher fuel utilization.

Keywords Membraneless microfluidic fuel cell · Concentration boundary layer · Dean vortices · Secondary flow · Mass transport

1 Introduction

Novel microfluidic fuel cells have aroused enormous interest due to their possible application in portable electronic devices, such as laptops, mobile phones, wearables or clinical diagnostic devices (Bazylak et al. 2005; Chang et al. 2006; Choban 2004; Dyer 2002). They are an alternative to conventional batteries, because of their higher energy density, low weight and the ability to be used without charging for a long period of time (Choban 2004; Ferrigno et al. 2002). Since the electrochemical reactions take place on the surface of the electrodes, the miniaturization of fuel cells, and thus the increase in area-to-volume ratio, leads to an improvement in power density (Bazylak et al. 2005; Kjeang et al. 2009). However, mechanical limitations occur in the miniaturization of conventional fuel cells. One of the biggest

challenge and a high cost factor is the installation of a polymer electrolyte membrane (PEM) into a miniaturized fuel cell. Additional problems arise due to the long-term stability, ohmic losses of the membrane and the complex water management of the membrane (Choban 2004; Cohen et al. 2005). All these issues can be avoided using a membraneless microfluidic fuel cell, in which the fuel and oxidant are introduced into a microchannel with integrated electrodes and flow in parallel at low Reynolds number without convective mixing (Fig. 1) (Bazylak et al. 2005; Choban 2004; Cohen et al. 2005; Ferrigno et al. 2002; Hashemi et al. 2017).

The performance of the microfluidic fuel cell depends on electrochemical kinetics, ohmic resistance and mass transport losses. Since the first published work in 2002 by Ferrigno et al. (2002) numerous studies, which consider several types of microfluidic fuel cells, different fuels and oxidants, various channel geometries and materials for the electrodes, were published in the field of microfluidic fuel cell technology. A very good overview of these studies can be found in Kjeang et al. (2009), Mousavi Shaegh et al. (2011) and Nasharudin et al. (2014). However, it is still difficult to commercialize microfluidic fuel cells due to insufficient power

✉ Wiebke Rösing
Wiebke.roesing@tu-ilmenau.de

¹ Institute of Thermodynamics and Fluid Mechanics,
Technische Universität Ilmenau, Am Helmholtzring 1,
98693 Ilmenau, Germany

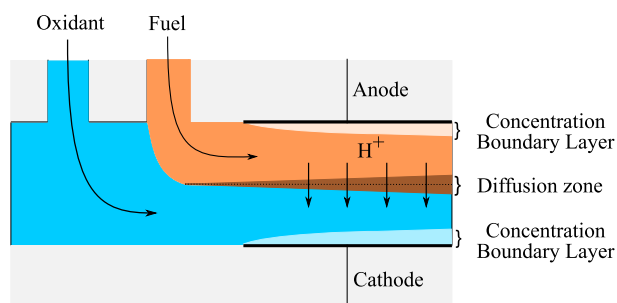


Fig. 1 Schematic of the membraneless microfluidic fuel cell

densities and poor fuel utilizations below 10%, which persist at practical flow rates and useful cell voltages (Kjeang et al. 2009). This is mostly caused by the formation of concentration boundary layers at the electrodes (Fig. 1). These concentration boundary layers result from the consumption of fuel and oxidant at the anode and the cathode, respectively and expand into the microchannel because of the diffusion-limited mass transport in the purely laminar flow regime. Therefore the continuous conversion of fuel and oxidant at the electrodes is hindered and result in insufficient power densities and low fuel utilizations. In order to increase the flux through the concentration boundary layer, a decrease in the thickness of the layer is required to create a steep concentration gradient, which leads to high reaction rates at the electrodes and thus to an improved performance of the microfluidic fuel cell (Chohan 2004; Ebrahimi Khabbazi et al. 2010). A possibility to reduce the size of the concentration boundary layers is to increase the flow rate. However, this results in a further decrease in fuel utilization, due to a shorter residence time of the fuel and oxidant at the respective electrode. Alternative methods for the suppression of the concentration boundary layer expansion in an active or passive way have been reported by Mousavi Shaegh et al. (2011), Da Mota et al. (2012) and Yoon et al. (2006). For example, Yoon et al. (2006) investigated three different setups for controlling the concentration boundary layers. They positioned multiple inlets or multiple outlets along the microchannel with integrated electrodes to supply the concentration boundary layer with fresh reactant or to remove the depleted fluid, respectively. However, this active control of the concentration boundary layer requires more energy for the fluidic pumping, because of the high pressure drop resulting from the sophisticated microfluidic channel design with very small in- and outlets, which yields a low overall efficiency of the fuel cell. Additionally, they investigated a passive control method using herringbone ridges to induce a transversal secondary flow, which refreshes the concentration boundary layer. For such passive methods no additional equipment is necessary. This method for reducing the concentration boundary layer in microfluidic fuel cells

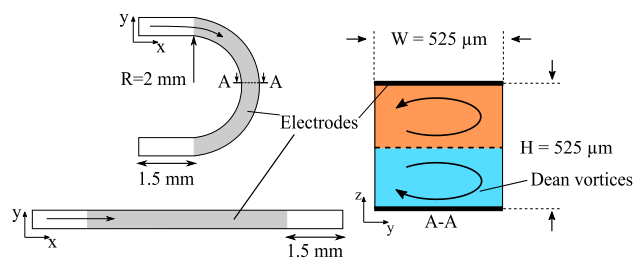


Fig. 2 Schematic representation of the curved and straight microfluidic fuel cell used in this study with induced counter-rotating vortices known as Dean vortices

has been optimized in several studies by investigating different geometrical parameters such as length and orientation of the ridges (Da Mota et al. 2012; D'Alessandro and Fodor 2014; Ha and Ahn 2014; Lee and Ahn 2015; Marschewski et al. 2015). However, the small herringbone structures in the microchannels increase the complexity of the manufacturing process and increase the possibility for trapping air bubbles, which lowers the overall efficiency (Howell et al. 2004). Another very simple method to transport fresh reactant from the middle of the channel towards the electrodes utilizing a transversal secondary flow without having the very complex and small structures of herringbone ridges is a curved microchannel (Rossi and Kähler 2014). In such microchannels two counter-rotating vortices arise, the so called Dean vortices (Fig. 2) (Sudarsan and Ugaz 2006a, b).

The counter-rotating vortices appear because the faster fluid in the middle of the curved channel part is pushed outwards, while the slower fluid near the electrodes will be displaced, due to continuity. The strength of the Dean vortices can be characterized by the Dean number De (Dean 1928)

$$De = Re \sqrt{\frac{D_h}{2R}}. \quad (1)$$

The Dean number depends on the radius of curvature R , the Reynolds number Re and the channel geometry expressed in terms of the hydraulic diameter D_h . The Reynolds number is given by the following equation:

$$Re = \frac{\rho v D_h}{\mu}, \quad (2)$$

where ρ is the density of the fluid, v the fluid velocity and μ the dynamic viscosity of the fluid. The Dean vortices induced by curved microchannels are already used in micromixers for applications where an intensive mixing or reaction of the two parallel streams is necessary (Howell et al. 2004; Jiang et al. 2004; Sudarsan and Ugaz 2006b). However, in microfluidic fuel cells a controlled supply of reactant towards the electrodes is required, which can be easily achieved by adjusting the strength of the transversal flow

by the variation of the Reynolds number for a channel with given radius of curvature. Xuan et al. (2011) already studied the mass transport of a two-layer laminar flow in curved microchannels using different *Re* and channel aspect ratios by computational fluid dynamic simulations. They found that at properly selected parameters the mass transport at the liquid–liquid interface can be reduced, so that curved microchannels can be used also for co-laminar microfluidic devices, such as microfluidic fuel cells (Xuan et al. 2011).

However a detailed study of curved microfluidic fuel cells as a novel, low cost and more efficient fuel cell, including the fluid dynamics and the electrochemical kinetics is still missing. For that reason the performance of a straight and a curved microfluidic fuel cell were compared in detail by numerical simulations, in order to characterize the influence of the Dean vortices on the performance of a microfluidic fuel cell. Therefore, a numerical model is applied including fluid dynamics, charge conservation, mass transport and chemical reaction kinetics with appropriate boundary conditions. Furthermore, a partly curved microchannel with integrated segmented electrodes in the straight and the curved channel part was fabricated. This enables a comparison of the electric current density of a model redox system, such as ferrocyanide/ferricyanide, obtained without the influence of Dean vortices in the straight channel part and with the enhanced mass transport induced by the Dean vortices in the curved channel part. This experiment answers the question, if the presented concept is a feasible alternative to current fuel cell designs.

2 Numerical model

2.1 Theory and simulations

The performance of a straight and a curved microfluidic channel, shown in Fig. 2, with the same channel length and electrode area was compared by numerical simulations. The fuel is set to be 0.5 M formic acid and the oxidant is 0.01 M potassium permanganate, both in 0.1 M H₂SO₄ aqueous solution. To simulate the fluid dynamics, charge conservation, species transport and chemical reactions, a 3D numerical model is applied in COMSOL using the parameters listed in Table 1.

2.1.1 Fluid dynamics

For the fluid flow, the continuity equation (3) and the Navier–Stokes equations (4) were solved for an incompressible, laminar flow at steady state and isothermal conditions:

$$\nabla \cdot \vec{v} = 0, \tag{3}$$

$$\rho(\vec{v} \cdot \nabla)\vec{v} = -\nabla p + \mu\Delta\vec{v}. \tag{4}$$

Table 1 Input values for the numerical simulations

Parameter	Value
Fuel concentration $c_{0,a}$	500 (mol m ⁻³)
Oxidant concentration $c_{0,c}$	10 (mol m ⁻³)
Diffusion coefficient D_a	1.5 × 10 ⁻⁹ (m ² s ⁻¹)
Diffusion coefficient D_c	1.6 × 10 ⁻⁹ (m ² s ⁻¹)
Exchange current density $j_{0,a}$	100 (A m ⁻²)
Exchange current density $j_{0,c}$	1 (A m ⁻²)
Charge transfer coefficient α	0.5
Stoichiometric coefficient ϑ_a	1
Stoichiometric coefficient ϑ_c	1
Density ρ	1000 (kg m ⁻³)
Dynamic viscosity μ	0.001 (kg m ⁻¹ s ⁻¹)
Faraday constant F	96,485.34 (C mol ⁻¹)
Temperature T	298 (K)
Universal gas constant R	8.314 (J mol ⁻¹ K ⁻¹)

Here, ρ is the fluid density, \vec{v} is the velocity, p the pressure and μ the dynamic viscosity. Since the *Re* number is 52.9 at most, the laminar flow module was used. No-slip boundary condition was applied at the channel walls. A mass flow was fed to the inlet and the pressure at the outlet was set to have a zero gauge pressure.

2.1.2 Charge conservation

In the electrolyte and at the electrodes charge conservation was set. Due to the supporting electrolyte, the electric field in the electrolyte can be described by (Ebrahimi Khabbazi et al. 2010):

$$\nabla \cdot (-\sigma_1 \nabla \phi_1) = 0. \tag{5}$$

σ_1 is the electric conductivity and ϕ_1 is the electric potential in the electrolyte. The electric potentials at the electrode surfaces ϕ_s were applied as boundary conditions. At the other boundaries the electric insulation boundary conditions were assigned. At the electrode–electrolyte interface the following equation for the activation overpotential η was applied (Tanveer and Kim 2017):

$$\eta = \phi_s - \phi_1 - E_{eq}, \tag{6}$$

where E_{eq} refers to the equilibrium potential of the respective reaction.

2.1.3 Mass transport and chemical reaction

The calculated solution for the velocity field was used to model the mass transport by a diffusion–convection equation for both species:

$$\nabla \cdot (D\nabla c - c\vec{v}) = 0, \tag{7}$$

where c and D are the concentrations and diffusion constants for fuel and oxidant. The transport of dilute species module was used. At the inlet a laminar flow profile was imposed. At one half of the inlet (anode) the concentration conditions $c_a = c_{0,a}$; $c_c = 0$ and at the other half of the inlet (cathode) the concentration conditions $c_c = c_{0,c}$; $c_a = 0$ were applied to feed the fuel and the oxidant. At the outlet there is a zero pressure condition. The chemical reactions at the electrode surfaces and the fuel and oxidant consumption were modeled by adding a source term R_i to the right side of Eq. (7) (Chang et al. 2006):

$$\nabla \cdot (D\nabla c - c\vec{v}) = R_i, \tag{8}$$

$$R_i = \frac{\vartheta_i}{nF} j_i, \tag{9}$$

where ϑ_i is the stoichiometric coefficient, n the number of transferred electrons, F the Faraday constant and j_i the local current density, which was determined by the concentration dependent Butler–Volmer equation (Chang et al. 2006):

$$j_i = j_{i,0} \frac{C_i}{C_{i,0}} \left[e^{\frac{\alpha n F}{RT} \eta} - e^{-\frac{(1-\alpha)n F}{RT} \eta} \right]. \tag{10}$$

In the above equation $j_{i,0}$ is the exchange current density, α is the transfer coefficient rate, T is the temperature and R is the universal gas constant. For generating the polarization curves the anode is always grounded and the cell potential was applied as the solid phase potential ϕ_s at the cathode.

For the simulations, first the laminar flow field was estimated following by solving simultaneously the equation for the mass transport and reaction kinetics. To ensure the reliability of the numerical results, a grid independence check was done. A user controlled mesh with the preset fine and with further mesh refinement near the walls in the form of three additional wall layers with about 228,000 elements was used for the calculation of the fluid flow. For the calculation of the mass transport of the species and the reaction kinetics a user controlled mesh with the preset fine and extra fine in the straight channel part and curved channel part respectively was used. Mesh refinement near the walls and near the diffusion zone in the form of 7 additional wall layers were added, resulting in a mesh with about 882,000 elements.

2.2 Validation

In order to validate the numerical results of this study, the model of Chang et al. (2006)—a 3 cm long straight channel with a cross section of $1000 \times 1000 \mu\text{m}^2$ and 2.1 M formic acid as fuel and 0.5 M oxygen as oxidant—was recreated. It is important to mention that Chang et al. (2006) modeled the electrodes as porous subdomains where diffusion and the chemical reactions took place without advection. In

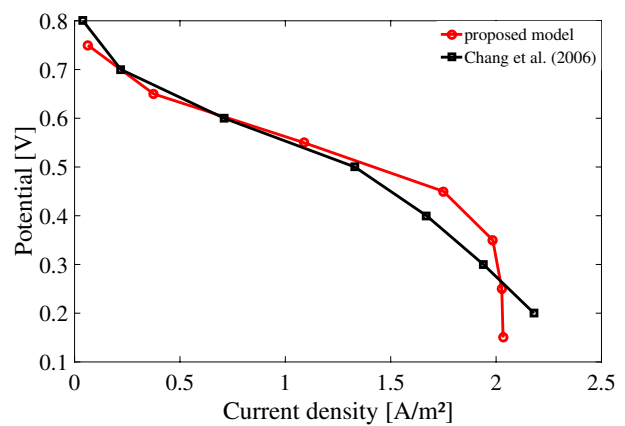


Fig. 3 Validation of the numerical results of the present model with the numerical model of Chang et al. (2006)

Table 2 Flow parameters used in the numerical simulations

Operating point	Flow rate (ml h ⁻¹)	Re	De
1	10	5.3	2.2
2	30	15.8	6.7
3	100	52.9	22.3

this study the electrodes were modeled as a surface using boundary conditions. Therefore, the standard exchange current density, where the true value is not known, was adjusted. This value depends on various factors, e.g., on the electrode surface roughness, orientation of the platinum crystals and the CO poisoning of the catalyst (Ebrahimi Khabbazi et al. 2010). For $j_{0,a}$ a value of 1 A m^{-2} and for $j_{0,c}$ a value of 0.03 A m^{-2} was used in the validation study. The other parameter used for the validation were similar to those reported by Chang et al. (2006). Although the electrodes were modeled differently, Fig. 3 shows a very good agreement between the calculated polarization curve and the polarization curve obtained by Chang et al. (2006). Therefore, this model was used to design the straight and the curved microfluidic fuel cell, shown in Fig. 2, using formic acid as fuel and potassium permanganate as oxidant.

2.3 Numerical results and discussion

The fluid flow, the evolution of the concentration boundary layer and the resulting current density were compared in the straight and curved microfluidic fuel cell by numerical simulations. Different flow rates were applied, corresponding to the three different operating points summarized in Table 2.

In Fig. 4, the numerical results of the velocity field in the two microchannels are depicted for the operating point 3 with the highest Reynolds number. The coordinate system

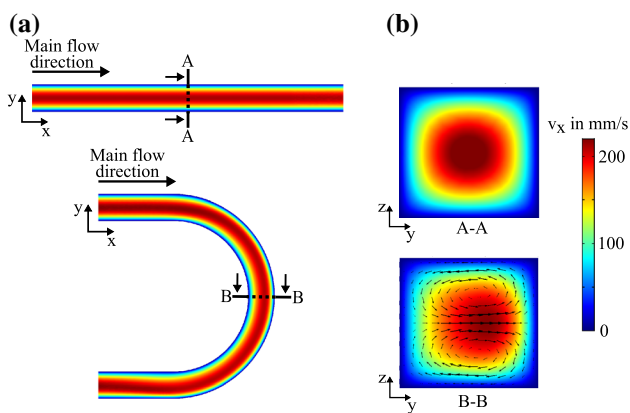


Fig. 4 **a** Numerically estimated main flow velocity v_x in the middle of the channel height at operating point 3. **b** Cross-sectional views of the velocity field in the straight and curved microfluidic fuel cell. The color represents the velocity v_x in streamwise direction, while the velocity vectors represent the transversal flow, non-existing in the straight, but well-pronounced in the curved microfluidic fuel cell (color figure online)

was oriented with the channel, i.e., x is always in streamwise direction, and y and z correspond to the channel width and

channel height direction, respectively. The cross-sectional view A–A shows the characteristic symmetrical velocity field in the straight microfluidic channel, where no transversal secondary flow is present. Whereas in the curved channel the maximum velocity in streamwise direction $v_{x,max}$ is shifted to the outer wall and thus a transversal secondary flow in y - and z -direction develops, which is indicated by the velocity vectors in Fig. 4b), cross section B–B. The maximum flow velocity of the transversal secondary flow in the curved channel part is $v_{y,max} \approx 21 \text{ mm s}^{-1}$ and $v_{z,max} \approx 10 \text{ mm s}^{-1}$ and thus by a factor of about 9.5 and 20 smaller than the flow in the streamwise direction. By decreasing the flow rate, which means a lower Dean number, the magnitude of the transversal secondary flow velocity in y - and z -direction decreases as well.

In Fig. 5a, the concentration distribution of the oxidant and the current density at the cathode along the straight microfluidic fuel cell at the three different operating points are shown. Due to the electrochemical reaction a concentration boundary layer is formed at the electrode. This boundary layer extends along the channel, ranging from 0 mM at the cathode to 10 mM in the bulk of the cathodic half-cell due to the diffusion-limited mass transport. The thickness

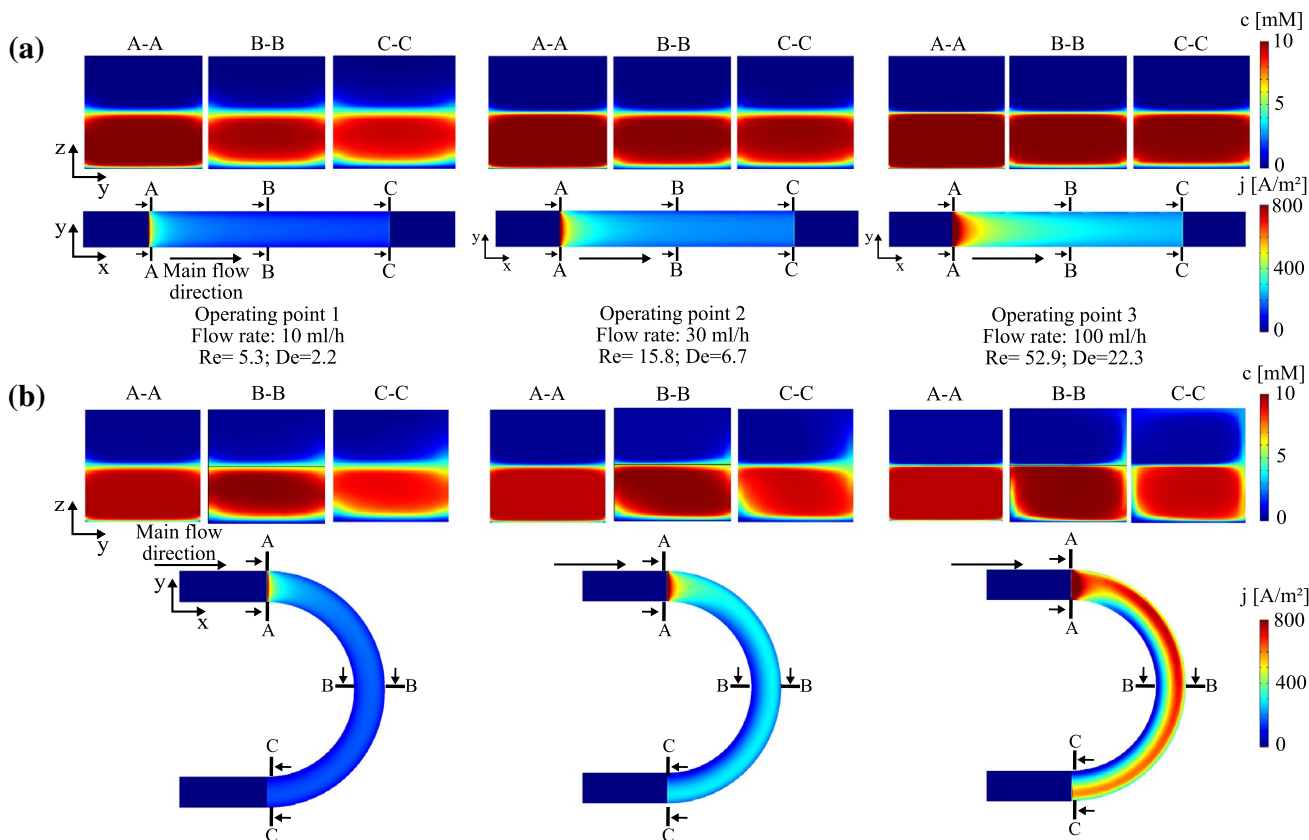


Fig. 5 Cross-sectional view of the potassium permanganate concentration at three different positions and evolution of the current density in the straight and **b** curved microfluidic fuel cell for three different operating points

of the concentration boundary layer increases with increasing channel length, which results in a strong decrease of the current density along the channel. An increased flow rate results in reduced concentration boundary layer thickness, and thus in a higher current density along the electrode surface. The maximum current density at the intersection B–B increases from 170.5 A m^{-2} at 10 ml h^{-1} (operating point 1) to 314.15 A m^{-2} at 100 ml h^{-1} (operating point 3) in the straight microfluidic channel. Furthermore, the thinner the concentration boundary layer thickness, the higher the concentration gradient. A higher concentration gradient results in higher chemical reaction rates, and thus in higher current densities. In the curved channel, the counter-rotating vortices develop and transport the depleted solution near the electrodes towards the inner side wall (negative y -direction) and supply the electrodes with fresh reactant as can be seen in Fig. 5b. This effect becomes larger at further downstream positions and at higher flow rates, and thus at higher Dean numbers. The deformation of the concentration boundary layer results in a high current density at the outer wall and a small current density at the inner wall of the curved electrode. At the intersection B–B the maximum and minimum current density at 10 ml h^{-1} is 173.58 A m^{-2} and 88.09 A m^{-2} . For a flow rate of 100 ml h^{-1} the current densities read 715.84 A m^{-2} and 50.48 A m^{-2} . So, the gain of the current density at the outer wall is higher than the loss at the inner wall, resulting in a much better performance of the curved microfluidic fuel cell compared to the straight microfluidic fuel cell, which can be seen by comparing the absolute values of current densities obtained for the flow rates 30 ml h^{-1} and 100 ml h^{-1} , depicted in Fig. 6.

Figure 6 shows the polarization curves for the straight and the curved microfluidic fuel cell at the three different operating points. The shape of the polarization curves is in agreement with polarization curves of a typical fuel cell, containing the initial potential drop due to activation losses,

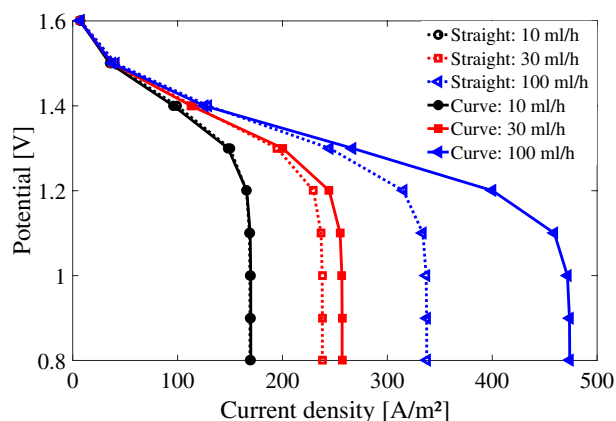


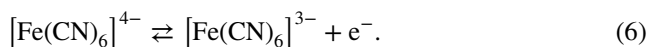
Fig. 6 Polarization curves for straight and curved microfluidic fuel cell at the three different operating points

the linear potential decrease at moderate current densities due to ohmic losses and the mass transport losses at high current densities. In this study the focus is on the mass transport losses, which are characterized by the strong voltage drop. This is due to the high reactant consumption rates at high current densities and the insufficient supply of reactants to the electrode surface, due to the diffusion-limited mass transport. The cell performance increases with increasing flow rate due to the increased mass transport. And, the higher the flow rate the higher the current density in the curved microfluidic channel. An increase of the current density of about 30% was obtained at a flow rate of 100 ml h^{-1} .

However, in microfluidic fuel cells care must be taken, because, due to the Dean vortices the diffusion zone, which arise at the interface between the oxidant and the fuel, is transported also to the electrodes so that a reactant crossover occurs, shown in Fig. 5b. For example, at the intersection C–C the oxidant concentration at the anode side increases at a flowrate of 10 ml h^{-1} from 7.9% in the straight channel to 8.2% in the curved channel and at a flowrate of 100 ml h^{-1} from 2.4% in the straight channel to 5.7% in the curved channel. Therefore, in microfluidic fuel cells the diffusive and convective mass transport has to be well-balanced to get a higher power density in the curved microfluidic channel compared to the straight microfluidic channel.

3 Experiment

In order to validate the improvements due to the curved channel obtained with numerical simulations, a curved microchannel with segmented electrodes in the straight and curved part was fabricated (see Fig. 7 and details in Sect. 3.3.1). To investigate the influence of the Dean vortices on the mass transport, and thus on the current response in the straight and curved channel part of the microfluidic device, electrochemical measurements were performed using the redox pair ferrocyanide/ferricyanide, which is a well-known 1-electron, reversible redox system and often used as a model system in electrochemical experiments (Van Benschoten et al. 1983):

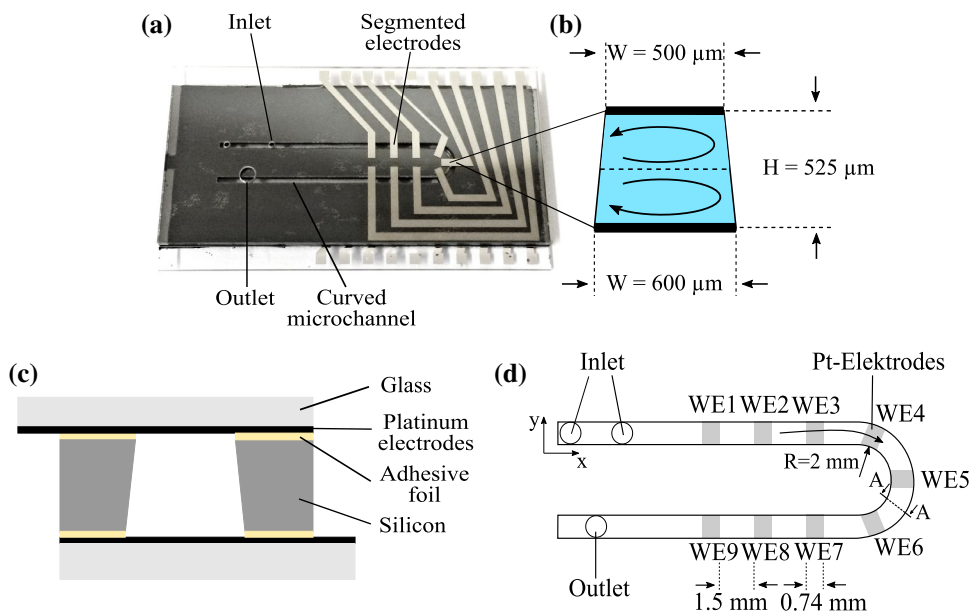


3.1 Experimental methods

3.1.1 Fabrication of the microfluidic device

The fabricated microfluidic device consists of a curved microchannel with segmented electrodes on the top and the bottom of the channel (Fig. 7). First, a $525 \mu\text{m}$ thick silicon

Fig. 7 **a** Photograph of the microfluidic device with segmented platinum electrodes on the top and the bottom of a silicon based curved microchannel. **b** Cross-sectional view of the microchannel with sketched Dean vortices. **c** Architecture of the microfluidic device. The trapezoid shape is due to the etching profile of the DRIE process. **d** Schematic representation of the curved microfluidic channel with segmented working electrodes (WE) used in this study



wafer was patterned by photolithography using AZ9260 photoresist. The patterned silicon wafer was etched completely through by plasma etching (DRIE). After this, the photoresist was removed. Due to the fabrication method the cross section has a trapezoid shape as depicted in Fig. 7c). For the fabrication of the electrodes an adhesion layer of 5 nm titanium following by 40 nm of platinum was deposited on top of two 500 μm thick glass wafers (Borofloat 33) via electron beam evaporation applying and using a shadow mask. Holes for the fluidic access were drilled into the top glass by a focused laser beam. The glass wafers were attached to the silicon wafer using an adhesive foil (PET adhesive film from Ritrama S.p.A, Italy). For this reason, the microchannel pattern was cut into the adhesive foil and aligned on both sides of the silicon wafer. The glass wafers were pressed on the top and bottom side of the silicon wafer. Classical bonding techniques such as anodic bonding are not possible in this case, due to the necessity of both-sided bonding. Finally, the wafer assembly was cut into chips. The electrical contact is given by protruding contact pads on the glass slides.

3.1.2 Electrochemical testing

The experimental studies were performed at room temperature using 5 mM of potassium hexacyanoferrate(II) trihydrate and 5 mM of potassium hexacyanoferrate(III) (both from Sigma Aldrich 99% ACS grade) dissolved in 1 M potassium chloride (ORG Laborchemie GmbH, 99.5% ACS grade) in 18 Ω-cm Millipore water. The solution was introduced via Polyethylene tubing by a syringe pump (neMESYS, Cetoni GmbH) into one inlet of the microfluidic chip, while the other inlet was closed. The electrochemical experiments were conducted using a bipotentiostat (VSP-300, Biologic

Science Instruments) in a three-electrode setup. The on-chip pseudo reference electrode (RE) was positioned upstream of the WEs and the counter electrode (CE) was placed externally in the outlet reservoir. Experiments were conducted several times in three independent microfluidic devices. All experimental measurements show the same results with only a few outliers at each experiment. The reason for the very few outliers is not clear so far, but might be due to gas bubbles in the microchannel, poor electrical contact, protruding adhesive foil into the microchannel or due to the fact that some electrodes dissolve from the glass surface during the experiments. For future systems the robustness of the system has to be improved. Here, the results of the measurements in one of the three fabricated channels are shown exemplary. In order to generate the current ratios, depicted in Fig. 10, a fifth order one-dimensional median filter was applied on the current response of the chronoamperometric measurements. The calculation of the mean value of the current response was done between 20 and 30 s after starting the chronoamperometric measurements.

3.2 Experimental results and discussion

First, cyclic voltammetry experiments were done to prove the performance of the fabricated microfluidic device using ferrocyanide/ferricyanide. Figure 8 shows cyclic voltammograms (CV) obtained at WE1 in 5 mM ferrocyanide and 5 mM ferricyanide using 1 M KCl as supporting electrolyte at 50 mV s⁻¹ scan rate and different flow rates. The CV measured at 0 ml h⁻¹ shows the oxidation and reduction peak of ferrocyanide and ferricyanide with a peak to peak separation of 102 mV. This indicates a not completely reversible redox reaction, which could be due to an electrode

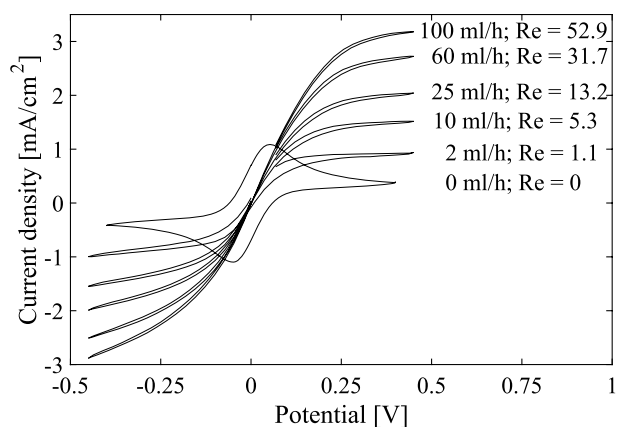


Fig. 8 Cyclic voltammograms obtained with 5 mM of potassium ferrocyanide and 5 mM of potassium ferricyanide from the microfluidic channel at increasing flow rates from 0 to 100 ml h⁻¹. Data were acquired at working electrode 1 (WE1) and a scan rate of 50 mV s⁻¹ using 1 M KCl as supporting electrolyte

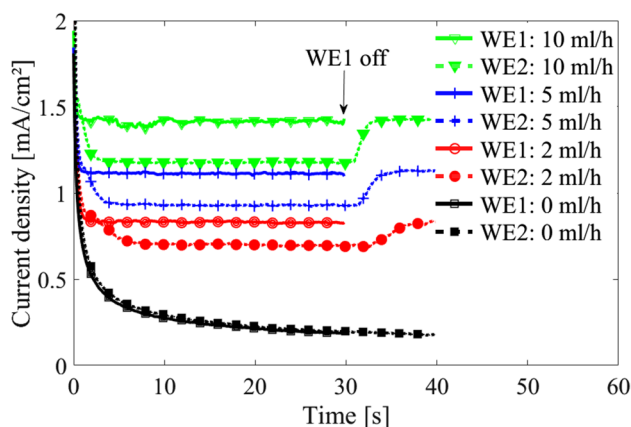


Fig. 9 Chronoamperograms in 5 mM potassium ferrocyanide and 5 mM potassium ferricyanide in 1 M KCl measured simultaneously at working electrode 1 (WE1; solid line) and WE2 (dotted line) at different flow rates using a bipotentiostat

surface modification during the experiments. However, the performance of the microfluidic device is successfully demonstrated. Increasing the flow rate means an increased mass transport towards the electrode, which results in an increasing steady state current density as can be seen on Fig. 8 for a potential of about 0.4 V.

Furthermore, chronoamperometry was performed to show the effect of the concentration boundary layer generated at WE1 on the current density of WE2. Figure 9 shows the resulting curves of the electrical current density measured simultaneously at WE1 and WE2 in 5 mM ferrocyanide and 5 mM ferricyanide in 1 M KCl at a potential of 0.4 V, and applying different flow rates. WE1 is switched off after 30 s to allow for dissipation of the concentration boundary layer

and to observe the evolution of the current density at WE2. At a potential of 0.4 V, the $\text{Fe}(\text{CN})_6^{4-}$ oxidizes and results in $\text{Fe}(\text{CN})_6^{3-}$, which diffuses into the bulk solution. Thus, an expanding depletion layer of ferrocyanide arises at the electrodes. At a zero flow rate (0 ml h⁻¹) the current density of WE1 and the current density of WE2 are equal since their surface areas are the same. Applying a flow results in a higher current density. However, the current density of WE2 is lower than the current density of WE1, because the concentration boundary layer formed at WE1 results in depleted solution at WE2 that can be oxidized. This effect leads to a reduced current density along the straight channel part in the microfluidic device. The influence of the concentration boundary layer starts earlier at higher flow rates, because the depleted solution reaches the WE2 earlier. After switching off the WE1, the current density at WE2 increases and reaches its initial value. By analyzing the temporal shift of the current steps of WE2 after switching off WE1, a typical convection velocity can be estimated (1) 2 ml h⁻¹: 0.2 mm s⁻¹, (2) 5 ml h⁻¹: 0.29 mm s⁻¹, (3) 10 ml h⁻¹: 0.47 mm s⁻¹. The estimated convection velocities, however, are much smaller than the estimated mean velocities within the microchannel, since the concentration boundary layer evolves close the wall where the no-slip condition holds, causing very slow velocities in vicinity of the electrodes; see Fig. 4b.

The chronoamperometric measurements were repeated for different electrodes with different downstream positions. Each time a potential of 0.4 V was applied at WE1 and simultaneously on a second electrode, either in the straight channel part before (WE2) and after the curve (WE8), where no secondary flow is present. Further measurements were conducted in the curved section using WE4, WE5, WE6 as second electrode. In this way the effect of the secondary flow on the electrochemical reaction can be investigated. In addition, numerical simulations were done and compared with the experimental results. For the numerical simulation the microfluidic device, sketched in Fig. 7d, with an ideal quadratic cross-sectional area of 525 μm × 525 μm was considered. 5 mM ferrocyanide was fed into the inlet assuming to have the same properties as water (density $\rho = 1000 \text{ kg m}^{-3}$; dynamic viscosity $\mu = 10^{-3} \text{ kg m}^{-1} \text{ s}^{-1}$). The diffusion coefficient was set to $D = 0.7 \times 10^{-9} \text{ m}^2 \text{ s}^{-1}$, corresponding to ferrocyanide dissolved in water (Stackelberg et al. 1953) and the exchange current density was set to 200 A/m². At the electrodes a solid phase potential ϕ_s of 400 mV was applied like in the experiment.

In Fig. 10, the resulting current ratios normalized by the current at 0 ml h⁻¹ for different Dean numbers are depicted for the experiment and for the simulation. For better visibility, only the current ratios obtained at WE2, WE5 and WE8 from the simulation were selected for comparison and shown dashed line in Fig. 10. For the uncertainty analysis

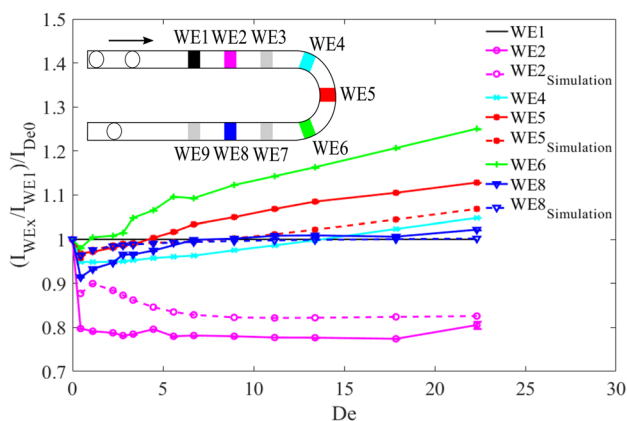


Fig. 10 Experimental and numerical results for the ratio of the current measured simultaneously at one working electrode (WE) at different positions to the current at WE1 normalized towards the current at stagnant flow conditions. Data were obtained by applying a potential of 400 mV in 5 mM potassium ferrocyanide and 5 mM potassium ferricyanide using 1 M KCl as supporting electrolyte with various flow rates resulting in Dean numbers ranging from 0 to 22

the standard deviation for the mean value of the absolute current measured in the chronoamperometric experiment was calculated and depicted as error bars in Fig. 10. The normalization of the current ratios allows a direct conclusion to an enhancement for values > 1 or a decrease of the current density for values < 1. The experimental results show that the formation of the concentration boundary layer at the first WE1 leads to a decrease of the current of about 23% at WE2, which is positioned next to WE1 in the straight channel part of the microfluidic electrochemical device. This current ratio remains almost constant, even though a higher flow rate is applied, since no Dean vortices evolve at the position of WE2. From the numerical result a drop of the current ratio at WE2 of about 17% occurs only, which is smaller compared to the experimental result. Besides a small deviation at low Dean numbers the current ratio is almost constant at higher De numbers, confirming qualitatively the behavior of the current density at WE2 measured in the experiment. Measuring the current ratio in the curve at WE4 (cyan), WE5 (red) and WE6 (green), an increasing current ratio with increasing Dean number occurred. This is due to the induced Dean vortices, causing a convective mass transport to the electrodes and, hence, a higher electrochemical reaction rate. This effect becomes larger at the electrodes with further downstream position as can be seen by the increase of the current ratio of WE5 and WE6 located in the middle and at the end of the curve, respectively. This is due to the fact that the displacement of depleted solution near the electrode at WE6 progressed further compared to WE5, which was already shown by the result of the numerical simulation done for the microfluidic fuel cell with only a curved microchannel; see Fig. 5b. For example,

the enhanced mass transport at $De = 13$ results in a current increase of about 7% and 14% at WE5 and WE6, respectively, compared to the current at WE1. This effect becomes larger at higher Dean numbers, which is also in agreement with the numerical results obtained for the fuel cell with only a curved microchannel; see Fig. 5b. The numerical result for the current ratio calculated at WE5 shows the same behavior. With increasing Dean number the current ratio increases and exceeds the current ratio at WE1 for $De > 8$. Besides, the absolute values of the current ratio are about 2.25% lower compared to the experimental results measured at WE5. The current ratio measured at WE8 reaches the current ratio of WE1 at $De = 5.6$, because at this point the concentration boundary layer formed at WE1 is completely displaced. Thus, the concentration distribution at WE8 is similar to the concentration distribution at WE1, resulting in the same current ratio, independently of the Dean number, as no transversal flow exists in the straight channel part. The experimental result of the current ratio measured at WE8 is in very good agreement with the numerical result. The current ratio calculated at WE8 reaches the current ratio of WE1 also at $De = 5.6$ and remains constant for higher Dean values. Only at small Dean numbers slight deviations occur. The different trends of the current ratio for low Dean numbers at the different electrodes measured in the experiments and calculated in numerical simulation could be due to the use of a microfluidic channel with trapezoid cross section for the experiment; see Fig. 7. At the current state, the manufacturing process does not allow to fabricate an ideal 525 μm deep microfluidic channel with perpendicular sidewalls as used for the simulation. Furthermore, a surface roughness of the sidewalls of about 5–20 μm exists, which cause, in conjunction with a partly protruding adhesive foil at some positions, more complex and unpredictable flow structures of three-dimensional characteristic, making it difficult to compare the numerical and experimental results quantitatively. However, the qualitative behavior of the current ratios agrees well, especially at higher Dean numbers, and corroborate the concept of utilizing Dean vortices to reduce the size of the concentration boundary layers, in order to increase the current density in microfluidic fuel cells.

4 Conclusion

In this paper a passive method for decreasing the size of concentration boundary layers, and thus improving the performance of microfluidic fuel cells was investigated. The idea is to use a curved microfluidic channel, which induces counter-rotating vortices to enhance the diffusion-limited mass transport towards the electrodes. The numerical results show that a significant higher performance of the fuel cell can be achieved, by using a curved microfluidic

channel instead of a straight one. For the chosen fuel cell, an increase of the current density of 8% is obtained at low flow rates (30 ml h⁻¹). At higher flow rates (100 ml h⁻¹) the increase of the current density amounted to 30%, due to much more pronounced counter-rotating vortices at higher flow velocities. Hence, much more fresh reactant is transported from the bulk towards the electrodes. However, care must be taken using curved microfluidic fuel cells. The diffusive and convective mass transport have to be well-balanced, in order to avoid a short circuit due to too strong Dean vortices, which transport also the inter-diffusion layer, containing oxidant and fuel, towards the anode and cathode.

The experimental results, obtained using a fuel cell with segmented electrodes along a microchannel with a curved section, clearly show the effect of the diffusion-limited mass transport on the current density. In the experiment the formation of a concentration boundary layer diminishes the electrochemical reaction, and thus decreases the current density along the straight part of the microchannel by about 23%. Due to the curved channel section, a transversal secondary flow is induced that enhances the mass transport and, therefore, increases the current density within the curve of the microchannel. This effect becomes larger at higher flow rates, and thus at higher Dean numbers. Although the fabricated fuel cell has some deficiencies, such as the adhesive foil, which protrudes at some positions into the channel, the experimental results corroborate the numerical ones. To investigate the critical point of the curved microfluidic fuel cell, namely the reactant crossover to the wrong electrode, in more detail, further experimental studies in an improved microfluidic fuel cell are needed using an optimized fabrication procedure. Furthermore, three-dimensional flow measurements should be carried out to resolve the counter-rotating vortices in the fabricated microfluidic fuel cells, which are, due to the optical access in between the segmented electrodes, well suited for three-dimensional flow measurements. In this way, the correlation between mass transport and transversal flow velocity can be directly revealed by comparing the local increase of the current density with the strength of the Dean vortices within the microchannel.

Acknowledgements This research was supported by Emmy-Noether Nachwuchsgruppe “Kontrollierte elektrochemische Energieumwandlung durch oberflächennahe Strömungsbeeinflussung” (CI 185/3). The authors also would like to thank Arne Albrecht and Michael Fischer and the staff of the DFG Center of Micro- and Nanotechnologies of the TU Ilmenau for the kind support in fabrication of the microfluidic fuel cell and Thomas Boeck (TU Ilmenau), Gerd Mutschke (Helmholtzzentrum Dresden Rossendorf), Kristina Tschulik (Ruhr University Bochum), Massimiliano Rossi (Bundeswehr University Munich) and Ingrid Fritsch (University of Arkansas) for fruitful discussions and suggestions.

Open Access This article is distributed under the terms of the Creative Commons Attribution 4.0 International License (<http://creativecommons.org/licenses/by/4.0/>), which permits unrestricted use, distribution, and reproduction in any medium, provided you give appropriate credit to the original author(s) and the source, provide a link to the Creative Commons license, and indicate if changes were made.

References

- Bazylak A, Sinton D, Djilali N (2005) Improved fuel utilization in microfluidic fuel cells: a computational study. *J Power Sources* 143:57–66. <https://doi.org/10.1016/j.jpowsour.2004.11.029>
- Chang M-H, Chen F, Fang N-S (2006) Analysis of membraneless fuel cell using laminar flow in a Y-shaped microchannel. *J Power Sources* 159:810–816. <https://doi.org/10.1016/j.jpowsour.2005.11.066>
- Chohan E (2004) Microfluidic fuel cell based on laminar flow. *J Power Sources* 128:54–60. <https://doi.org/10.1016/j.jpowsour.2003.11.052>
- Cohen JL, Westly DA, Pechenik A, Abruña HD (2005) Fabrication and preliminary testing of a planar membraneless microchannel fuel cell. *J Power Sources* 139:96–105. <https://doi.org/10.1016/j.jpowsour.2004.06.072>
- D’Alessandro J, Fodor PS (2014) Use of grooved microchannels to improve the performance of membrane-less fuel cells. *Fuel Cells* 14:818–826. <https://doi.org/10.1002/fuce.201400047>
- Da Mota N, Finkelstein DA, Kirtland JD, Rodriguez CA, Stroock AD, Abruña HD (2012) Membraneless, room-temperature, direct borohydride/cerium fuel cell with power density of over 0.25 W/cm². *J Am Chem Soc* 134:6076–6079. <https://doi.org/10.1021/ja211751k>
- Dean WR (1928) Fluid motion in a curved channel. *Proc R Soc Lond* 121:402–420
- Dyer CK (2002) Fuel cells for portable applications. *Fuel Cells Bull* 2002:8–9. [https://doi.org/10.1016/S1464-2859\(02\)80334-0](https://doi.org/10.1016/S1464-2859(02)80334-0)
- Ebrahimi Khabbazi A, Richards AJ, Hoorfar M (2010) Numerical study of the effect of the channel and electrode geometry on the performance of microfluidic fuel cells. *J Power Sources* 195:8141–8151. <https://doi.org/10.1016/j.jpowsour.2010.06.094>
- Ferrigno R, Stroock AD, Clark TD, Mayer M, Whitesides GM (2002) Membraneless vanadium redox fuel cell using laminar flow. *J Am Chem Soc* 124:12930–12931. <https://doi.org/10.1021/ja020812q>
- Ha S-M, Ahn Y (2014) Laminar flow-based micro fuel cell utilizing grooved electrode surface. *J Power Sources* 267:731–738. <https://doi.org/10.1016/j.jpowsour.2014.06.005>
- Hashemi S, Neuenschwander M, Hadikhani P, Modestino MA, Psaltis D (2017) Membrane-less micro fuel cell based on two-phase flow. *J Power Sources* 348:212–218. <https://doi.org/10.1016/j.jpowsour.2017.02.079>
- Howell PB Jr, Mott DR, Golden JP, Ligler FS (2004) Design and evaluation of a Dean vortex-based micromixer. *Lab Chip* 4:663–669. <https://doi.org/10.1039/b407170k>
- Jiang F, Drese KS, Hardt S, Küpper M, Schönfeld F (2004) Helical flows and chaotic mixing in curved micro channels. *AICHE J* 50:2297–2305. <https://doi.org/10.1002/aic.10188>
- Kjeang E, Djilali N, Sinton D (2009) Microfluidic fuel cells: a review. *J Power Sources* 186:353–369. <https://doi.org/10.1016/j.jpowsour.2008.10.011>
- Lee S-W, Ahn Y (2015) Influence of electrode groove geometry on the passive control of the depletion layer in microfluidic fuel cells. *J Micromech Microeng* 25:127001. <https://doi.org/10.1088/0960-1317/25/12/127001>
- Marschewski J, Jung S, Ruch P, Prasad N, Mazzotti S, Michel B, Poulidakos D (2015) Mixing with herringbone-inspired

- microstructures: overcoming the diffusion limit in co-laminar microfluidic devices. *Lab Chip* 15:1923–1933. <https://doi.org/10.1039/c5lc00045a>
- Mousavi Shaegh SA, Nguyen N-T, Chan SH (2011) A review on membraneless laminar flow-based fuel cells. *Int J Hydrogen Energy* 36:5675–5694. <https://doi.org/10.1016/j.ijhydene.2011.01.063>
- Nasharudin MN, Kamarudin SK, Hasran UA, Masdar MS (2014) Mass transfer and performance of membrane-less micro fuel cell: a review. *Int J Hydrogen Energy* 39:1039–1055. <https://doi.org/10.1016/j.ijhydene.2013.09.135>
- Rossi M, Kähler CJ (2014) Experimental characterization of the effect of dean vortices on microfluidic fuel cells. In: Proceedings of the 4th European conference on microfluidics, December 10–12, Limerick
- Stackelberg M, Pilgram M, Toome V (1953) Bestimmung von Diffusionskoeffizienten einiger Ionen in wässriger Lösung in Gegenwart von Fremdelektrolyten. *Zeitschrift für Elektrochemie* 57:342–350. <https://doi.org/10.1002/bbpc.195300073>
- Sudarsan AP, Ugaz VM (2006a) Fluid mixing in planar spiral microchannels. *Lab Chip* 6:74–82. <https://doi.org/10.1039/b511524h>
- Sudarsan AP, Ugaz VM (2006b) Multivortex micromixing. *Proc Natl Acad Sci USA* 103:7228–7233. <https://doi.org/10.1073/pnas.0507976103>
- Tanveer M, Kim KY (2017) Effects of geometric configuration of the channel and electrodes on the performance of a membraneless micro-fuel cell. *Energy Convers Manage* 166:328–336. <https://doi.org/10.1016/j.enconman.2017.01.027>
- Van Benschoten JJ, Lewis JY, Heineman WR, Roston DA, Kissinger PT (1983) Cyclic voltammetry experiment. *J Chem Educ* 9:772–776
- Xuan J, Leung MK, Leung DY, Ni M (2011) Density-induced asymmetric pair of Dean vortices and its effects on mass transfer in a curved microchannel with two-layer laminar stream. *Chem Eng J* 171:216–223. <https://doi.org/10.1016/j.cej.2011.01.011>
- Yoon SK, Fichtl GW, Kenis PJA (2006) Active control of the depletion boundary layers in microfluidic electrochemical reactors. *Lab Chip* 6:1516–1524. <https://doi.org/10.1039/b609289f>

Publisher's Note Springer Nature remains neutral with regard to jurisdictional claims in published maps and institutional affiliations.